reactions

MDPI

Article

Gas-Phase Reactions in Nano-Strand Formation from Al-Fe-Ni Powder Reacted with CaF_2-SiO_2-Al_2O_3-MgO-MnO-TiO_2 Flux at 1350 °C: SEM Study and Diffusion Calculations

Theresa Coetsee * and Frederik De Bruin

Department of Materials Science and Metallurgical Engineering, University of Pretoria, Pretoria 0002, South Africa; fjdb.1953@gmail.com

* Correspondence: theresa.coetsee@up.ac.za

Abstract: Fast high-temperature gas-phase reactions occurring in the limited space of the arc cavity in the submerged arc welding (SAW) process limit the study of specific gas-phase behaviours. A low-temperature experimental method is applied to investigate gas-phase reactions in the reaction of oxy-fluoride slag with Al-Fe-Ni metal powders. The presence of nano-strands in the slag cavities confirms the vaporisation and re-condensation of gasses. Ti is the main element in nano-strands, although some nano-strands also contain Al-Mg-Si-Na oxy-fluoride. Nano-strand end-caps contain Mn-Fe-Si fluoride, and some contain Ni. The Ni in nano-strand end-caps is sourced from the added Ni powder and indicates gas-phase transfer. The Ti in the nano-strands is sourced from the flux. Themochemistry calculations identify $KAlF_4$, TiF_3, $NaAlF_4$, SiF_4, AlF_3, SiF_3, and Na in the gas phase. Increased Al reaction results in decreased TiF_3 in the gas phase, likely due to the displacement of Ti from TiF_3, resulting in the gas-phase transfer of Ti from the flux. Comparative diffusion flux calculations support Ti nano-strand formation via the vaporisation of TiF_3 and the re-condensation of Ti. The low-temperature simulation experiment applied here can be used to study the gas reaction behaviour in the reaction of oxy-fluoride flux with metal powders.

Keywords: oxy-fluoride; nano; diffusion; flux; welding; slag; phase

Academic Editor: Dmitry Yu. Murzin

Received: 25 October 2024
Revised: 17 December 2024
Accepted: 31 December 2024
Published: 2 January 2025

Citation: Coetsee, T.; De Bruin, F. Gas-Phase Reactions in Nano-Strand Formation from Al-Fe-Ni Powder Reacted with CaF_2-SiO_2-Al_2O_3-MgO-MnO-TiO_2 Flux at 1350 °C: SEM Study and Diffusion Calculations. *Reactions* **2025**, *6*, 1. https://doi.org/10.3390/reactions6010001

1. Introduction

Several pyrometallurgical processes use fluoride-based slags to aid in the processing and refining of alloys. For example, oxy-fluoride slags are applied in ESR (electroslag refining), the continuous casting of steel, and welding processes such as submerged arc welding (SAW) [1]. Gas formation from the oxy-fluoride slag is well documented [2–8]. The effect of oxy-fluoride composition on the extent of fluoride vaporisation is poorly understood because the gas phase analysis is not easily measured. One exception is the study by Zaitsev et al. [2] on the vaporisation of CaF_2-SiO_2-CaO-Al_2O_3-Na_2O-K_2O mould powder heated continuously to 1527 °C. The gas vaporisation sequence measured from the gas analyses identified the initial formation of NaF at 600 °C and KF formation at 883 °C. SiF_4 formation started at 830 °C and increased linearly with increasing temperature. AlF_3 formed from 974 °C to 1200 °C. CaF_2 vaporisation occurred at temperatures higher than 1262 °C. The following gas species were also identified: $NaAlF_4$, Na_2AlF_5, BF_3, and AlOF [2].

Several studies have provided insights into the likely gas-phase reaction products formed in these experiments. The observation of mass loss from the experiments, in combination with thermodynamic analysis, was applied to explain the likely gas-phase reaction

products [3,4]. However, the conclusions often appear to be contradictory. For example, increased slag vaporisation was measured with increased TiO_2 content in CaF_2-CaO-Al_2O_3-MgO-Li_2O-TiO_2 ESR slags reacted at 1470 °C to 1530 °C [3], and decreased vaporisation was measured with increased Al_2O_3 content in mould flux reacted at 1400 °C. This mould flux contained 14% CaF_2 and an initial Al_2O_3 content of 4% [4]. Increased vaporisation was more pronounced at alumina contents higher than 22%. On the other hand, studies found increased vaporisation with increased CaF_2 in ESR slag (CaF_2-CaO-Al_2O_3-MgO-TiO_2) reacted at 1000 °C to 1500 °C, and in 1–9% CaF_2-containing slags containing the binary oxides of CaO-SiO_2, MgO-SiO_2, and Al_2O_3-SiO_2 when reacted at 1400 °C to 1600 °C [5,6]. The application of simplified reaction systems provides a better opportunity to deduce the likely gas-phase compounds formed from the oxy-fluoride slag. The formation of Ti-fluoride gas was confirmed from the interaction of Ti metal and individual fluorides of CaF_2, LiF, and MgF_2 heated to temperatures of 900 °C to 1280 °C in a 10^{-3} Pa vacuum [8]. The formation of gas-phase compounds in SAW is even more prevalent than in ESR and continuous casting because of the much higher temperatures prevailing in the arc cavity, up to 2500 °C [9,10]. The formation of fluoride-based gas species is designed to form a shielding gas that protects the weld metal from oxygen, nitrogen, and hydrogen pick-up from the air [1]. In addition, the added CaF_2 forms an oxy-fluoride slag in which the oxides are diluted to limit the release of oxygen in the arc cavity. It is well established that the oxides in the SAW flux decompose in the arc cavity to release oxygen [11–15]. This oxygen can quickly oxidise high oxygen affinity metals such as Ti and Cr, leading to decreased Ti and Cr element transfer into the weld metal [16]. The aluminium-assisted alloying of carbon steel was applied to improve the element transfer of Ti and Cr to the weld metal by lowering the oxygen partial pressure in the arc cavity and at the molten flux–weld pool interface [17]. In addition, combining aluminium with either Ti or Cr and other alloying elements such as Ni is essential in demonstrating the practical application of weld metal alloying via unconstrained metal powders (not flux-cored wire or metal-cored wire) [17]. Using flux-cored, metal-cored, or solid-alloyed wire requires added manufacturing steps in welding consumables production, thus increasing welding costs. Previous studies demonstrated that adding iron-based powder in SAW increases welding efficiency by increasing deposition rates for the same heat input applied as in only feeding the weld wire [18–21]. The added metal powder is easily melted because, in the normal SAW process, only 20% of the arc energy is used to melt the weld wire [21]. Although nickel does not easily oxidise and does not require much shielding from oxygen, as is the case for Ti and Cr, the benefit of adding nickel to pre-alloyed powder instead of solid-alloyed wire results in better weld metal composition control [22]. The work-hardening of high-nickel content wire complicates the manufacturing and the feeding of this wire through the SAW wire feeding system, leading to the development of flux-cored wires [23]. The benefit of aluminium addition in welding for its exothermic reaction with oxygen sources was demonstrated in various welding processes, such as in shielded metal arc welding (SMAW) and self-shielded flux-cored arc welding (FCAW-S) [24–27]. Aluminium is also added as a deoxidising and denitrification agent in self-shielded flux-cored wires to ensure non-porous welds by binding nitrogen from the air [28–30].

Extensive welding test work is required to develop modifications to the SAW process. A simplified test on the interaction between aluminium and alloying metal powders with welding flux will save many resources. The high temperatures in the arc cavity and the harsh conditions imposed by the arc plasma in the small arc volume formed in a few seconds make the product gas analysis difficult and require specialist equipment [31,32]. To this end, this work applies a low-temperature experimental method to investigate gas-phase reactions in the oxy-fluoride slag, specifically when reacted with Al-Fe-X metal powders.

The method simulates the oxy-fluoride slag behaviours in the SAW process, especially the gas formation and metal assimilation reactions observed in the aluminium-assisted SAW process. This method was successfully applied to investigate nano-strand formation in oxy-fluoride slag reacted with Al-Fe-Ti, Al-Fe-Cr and Al-Fe-Co metal powders [33–35]. In post-weld slags, the identification and chemical analyses of three-dimensional (3D) structures by scanning electron microscope (SEM) showed the formation of oxy-fluoride nano-strands in the slag cavities [36,37]. It was concluded that the nano-strands observed in the slag cavities formed from the re-condensation of arc cavity gasses. Similarly, nano-strands were identified in the low-temperature (1350 °C) reaction of Al-Fe-Ti, Al-Fe-Cr and Al-Fe-Co metal powder mixtures with CaF_2-SiO_2-Al_2O_3-MgO-MnO-TiO_2 flux. However, the nano-strand composition changed depending on the alloying metal powder added, namely Ti or Cr or Co [33–35]. It appears that the nano-strand formation behaviour changes with metal powder addition. Therefore, in this work, the study of nano-strand formation from the reaction of Ni-containing Al-Fe powder with the flux is of importance.

Thermochemistry calculations in the form of gas–slag–metal equilibrium calculations were applied to identify the gas-phase compounds formed in aluminium-assisted SAW [37,38]. The equilibrium calculations showed that Ni vapour is present in the gas phase at the high temperatures prevailing in the arc cavity [37]. The main gas species from the equilibrium calculation for conventional SAW at 2000 °C are CO, Na, NaF, CaF_2, MgF_2, MgF, AlF_3, AlF_2, $NaAlF_4$, TiF_3, and $KAlF_4$, and the minor gas species at less than 1% are K, KF, Mg, AlF, Mn, Fe, SiF_4, and SiO [38]. In the modified SAW process, aluminium was added as a de-oxidiser element to lower the oxygen partial pressure in the arc cavity and at the weld pool–slag interface to enhance the transfer of high oxygen affinity powdered metals such as Cr and Ti into the weld pool [14,36,37]. The equilibrium calculation for the aluminium-assisted SAW process at 2500 °C with added Al-Ni-Cr-Co-Cu metal powders identified the following gas species: Mg, AlF, Fe, Cu, N_2, CO, OAlF, SiO, Mn, Na, MgF, Cr, AlF_2, Al_2O, and Al [37]. The formation of similar fluoride gas compounds from oxy-fluoride slags reacted at the mild temperatures applied by Zeitsev et al. [2] and those calculated for the high temperatures in SAW indicates that a low-temperature simulation experiment should be adequate as a simulation experiment of the oxy-fluoride slag behaviours in the SAW process.

This work aims to identify and investigate the nano-strand formation behaviour of Ni added as Al-Fe-Ni metal powders to the welding flux. Nano-strands indicate the vaporisation and re-condensation of gasses containing the nano-strand composition elements. Thermochemistry calculations in the form of gas–slag–metal equilibrium calculations were used to determine the likely gas-phase compounds in the low-temperature reactions at 1350 °C. The likelihood of liquid slag-phase vs. gas-phase reactions in nano-strand formation is investigated via diffusion flux comparison calculations.

2. Materials and Methods

2.1. Materials

The flux used in this work corresponds to the flux used in previous welding experiments. The chemical composition is summarised in Table 1, with the iron oxide expressed as Fe_2O_3 [14,36–39]. The mineralogy and chemistry of this flux and its post-weld slag-phase chemistry were described elsewhere [39]. The slag phases include the liquid oxy-fluoride main phase and spinel crystals ($MgO{\cdot}Al_2O_3$) [39]. The flux agglomerate particle size was 0.2–1.6 mm.

Table 1. Bulk chemical composition of flux and pellet (mass%).

	%MnO	%CaO	%SiO_2	%Al_2O_3	%CaF_2	%MgO	%Fe_2O_3	%TiO_2	%Na_2O	%K_2O	%Al	%Fe	%Ni
Flux	7.0	0.1	20.2	25.7	18.5	22.9	2.7	1.0	1.7	0.2	0	0	0
Pellet	5.4	0.1	15.5	19.8	14.2	17.6	2.1	0.8	1.3	0.2	7.7	7.7	7.7

The added pure metal powders were sourced as follows: Al (99.7% Al, −1 mm) was supplied by Sigma-Aldrich (Johannesburg, South Africa), Ni (99.5% Ni, −250 µm) was supplied by Goodfellow (Cambridge, England), and Fe (96.0% Fe, −50 µm) was provided by Merck (Johannesburg, South Africa). The Fe powder was added to simulate the presence of Fe in the SAW of carbon steel, in which iron is sourced from the weld wire and base plate [14,36,37]. The Al and Ni powders are the same as those applied in the prior SAW work [14,36,37]. The calculated pellet composition is displayed in Table 1, resulting from 8 mass% of each metal powder added to 15 g of flux.

2.2. Methods

The experimental methods used in preparing and reacting the sample mixture are the same as those reported previously [33–35]. Sample preparation consisted of weighing and mixing the solid reactants of flux and metal powders. A cylindrical pellet was formed by applying a 10-ton load to the mixture in a 20 mm diameter mould. The mixture of 19.5 g compressed to 30 mm pellet height.

Before loading the pellet into the furnace, the pellet was placed onto the sample holder. The sample holder consisted of a low-carbon steel plate of dimensions of 70 mm square and 2 mm thickness. The sample holder had a pressed circular recessed centre to assist in pellet placement, as shown in Figure 1. A muffle furnace was pre-heated to 1350 °C and soaked for 12 h at 1350 °C. Following this soaking time, the sample holder and pellet were placed into the muffle furnace and reacted for 6 min. Upon completion of the reaction time, the pellet and sample holder were removed from the furnace to cool down in the air. The cooled pellet was sectioned through its middle, and the inner faces were coated with gold. The three-dimensional (3D) sample was analysed by scanning electron microscope (SEM). A Zeiss crossbeam 540 FEG (field emission gun) SEM with an energy-dispersive X-ray spectroscopy (EDX) probe operated at 20 kV was used to perform phase chemical analyses of the 3D sample. The Zeiss crossbeam 540 FEG SEM is supplied by Carl Zeiss Microscopy GmbH, Jena, Germany.

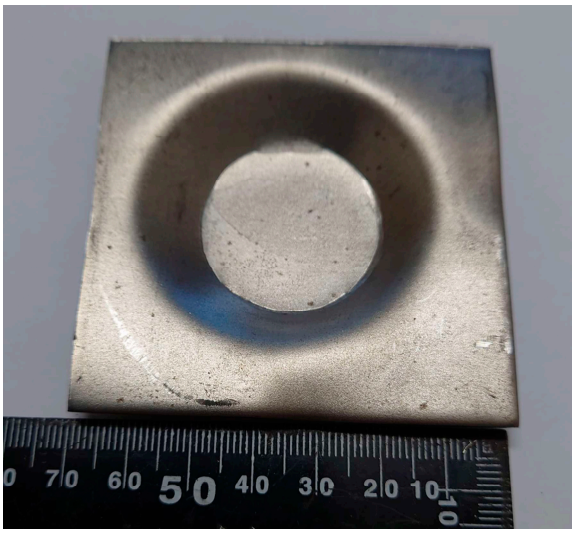

Figure 1. Sample holder.

3. Results

The SEM image in Figure 2 shows a slag cavity wall containing 3D features in the form of nano-strands and a sphere embedded in the cavity wall. At the higher magnification (×3520) in Figure 3, the nano-strands are better visible, showing the blocked field from Figure 2. The blocked field in Figure 3 is shown in Figure 4a, with the EDX element maps of the field of view (FOV) shown in Figure 4b. The nano-strands consist of Ti, and the nano-strand end-caps consist of Mn-Fe-Si fluoride. Some Ni is identified in the nano-strand end-caps, but the EDX map detail for Ni is faint. The formation of Ti nano-strands with Mn-Fe-Si fluoride end-caps appears similar to those previously identified [35]. The background matrix material consists of angular spinel crystals, presenting as Al-Mg-O phase areas, coated with Ca-Si-Na-K oxy-fluoride glass as expected from the phase chemistry of this particular flux [39]. Since the same flux was applied previously at 1350 °C and in welding experiments, the phase chemistry of the molten flux is as expected from prior work, namely solid spinel crystals embedded in the liquid oxy-fluoride glass phase [36,39]. The analysed glass phase chemistry in the post-weld slag is shown in Table 2 [39].

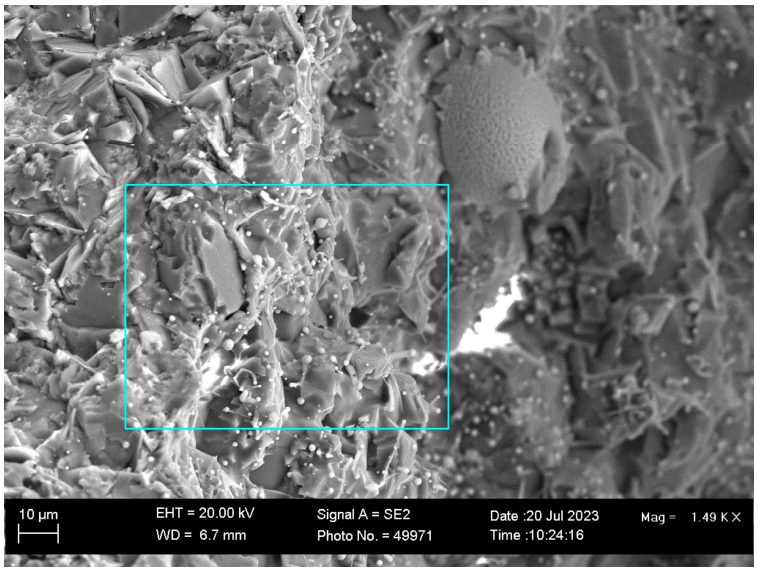

Figure 2. SEM image of nano-strands in slag cavity wall (×1490).

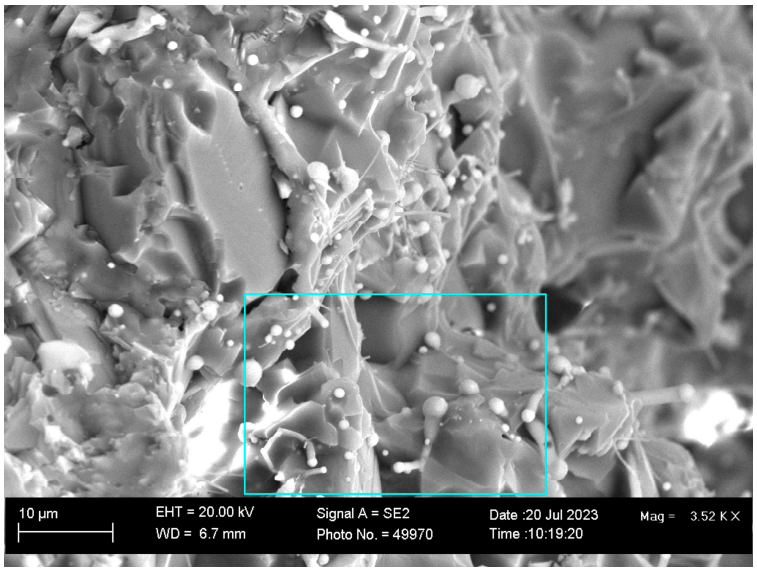

Figure 3. SEM image of nano-strands in the blocked area in Figure 2 (×3520).

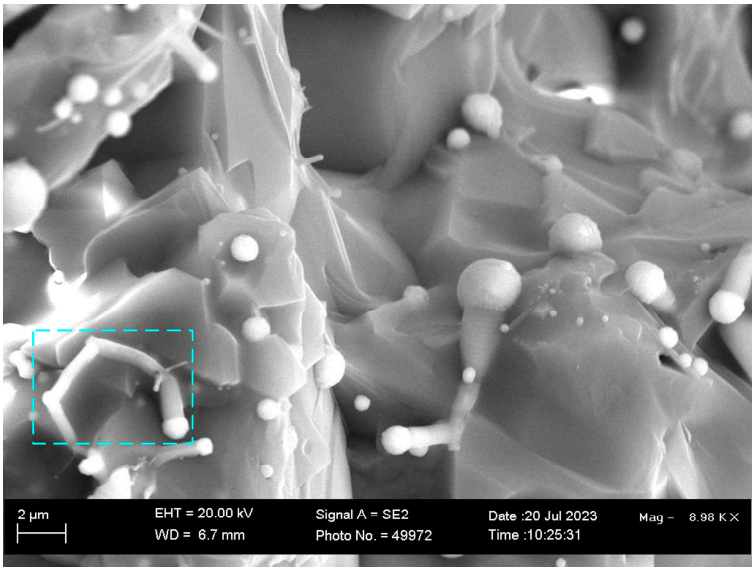

(**a**)

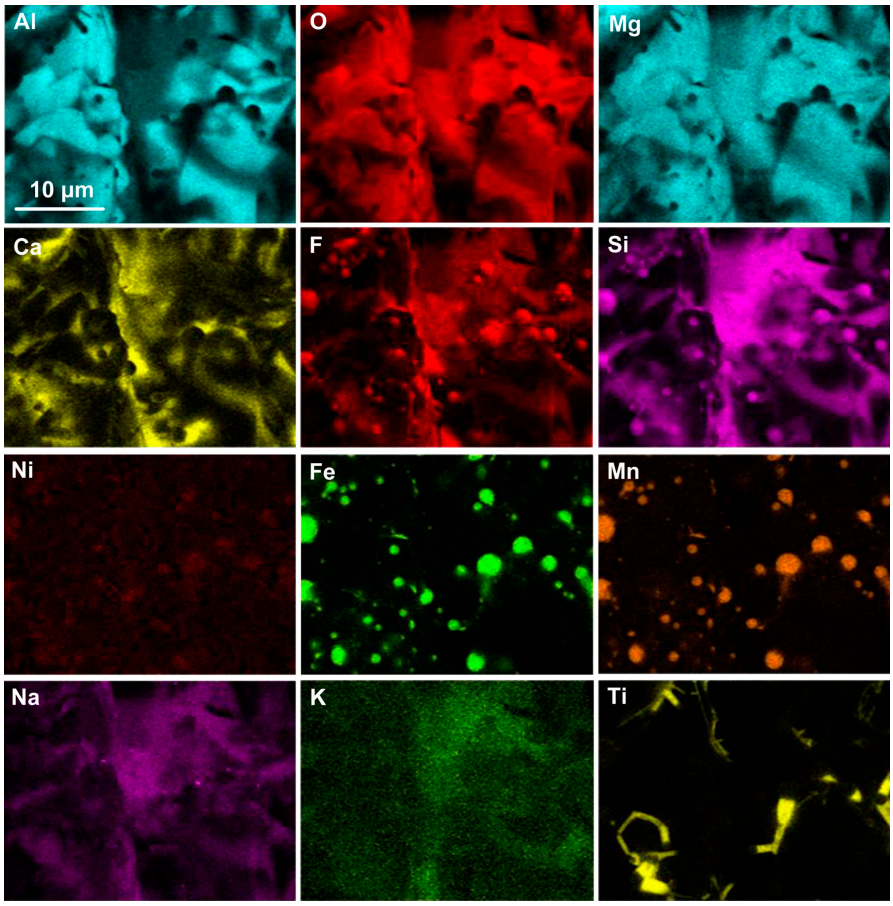

(**b**)

Figure 4. (**a**): SEM image (×8980) of analysed area marked as blocked area in Figure 3; (**b**): EDX map of area in (**a**).

Figure 5 illustrates nano-strands protruding from the cavity wall. Figure 6 shows the blocked field from Figure 5 at (×4420), and Figure 7a shows the blocked field from Figure 6 at (×12,260) with the FOV EDX maps displayed in Figure 7b. The large nano-strand in Figure 7 has the dimensions of a 0.5 µm diameter and 13 µm length. These dimensions appear larger than the nano-strand dimensions in Figure 4. For comparison, the c-shaped

nano-strand in Figure 4, marked as the dashed-line block in Figure 4a, is 8 μm in length and 0.8 μm in diameter at its thick end. Figure 7b shows that the nano-strand compositions are dominated by Ti, similar to the observation from Figure 4b. However, the nano-strands in Figure 7b also contain Al-Mg-Si-Na oxy-fluoride. This compositional variation is better displayed in the marked dashed-line oval area in Figure 7a, with the nano-strands viewed against the black slag cavity background. In comparison, the presence of elements in addition to Ti is not that clear in viewing the large nano-strand in the marked dashed-line blocked area against the matrix slag background. Both these variations in nano-strand composition were identified previously in the reaction of various metal powders with the same flux as applied here. Ti nano-strands were identified in the reaction of Co-Al-Fe metal powder [35], oxy-fluoride nano-strands containing Al-Mg-Ca-Si-Na-K were identified in the reaction with Cr-Al-Fe metal powder, and oxy-fluoride nano-strands containing Al-Mg-Si-Ti-Na were identified in reaction with Ti-Al-Fe metal powder [33,34].

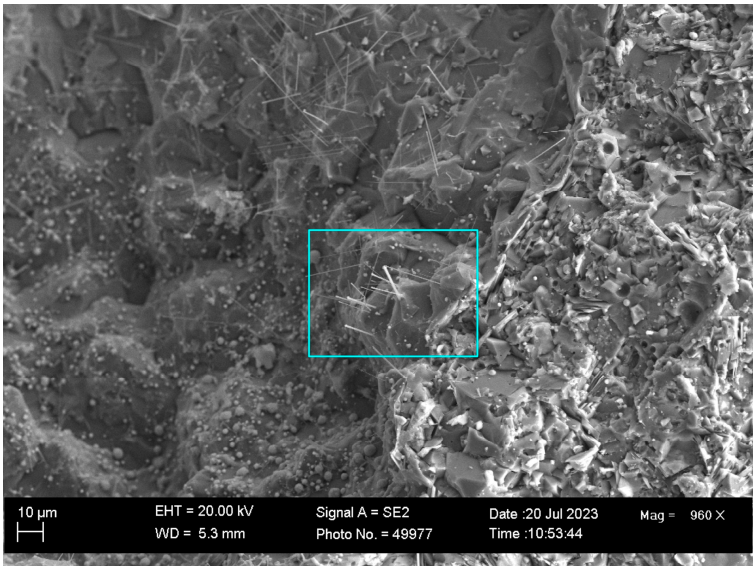

Figure 5. SEM image of nano-strands at slag cavity wall (×960).

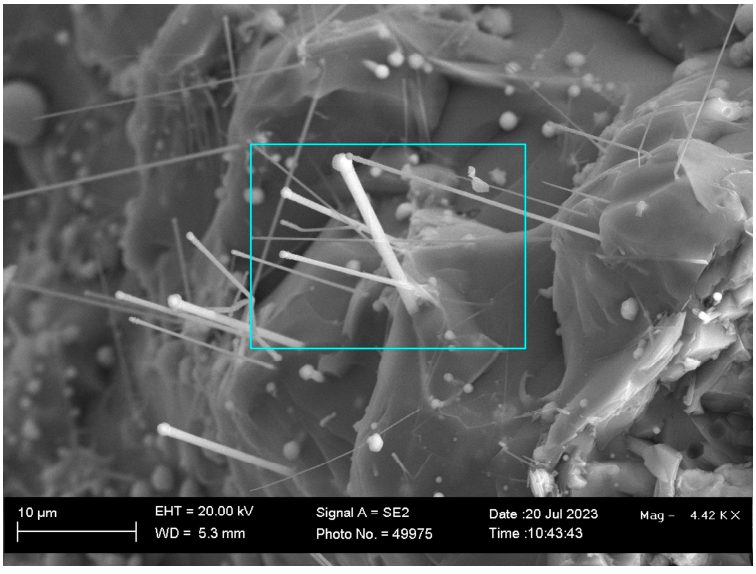

Figure 6. SEM image of nano-strands in the blocked area in Figure 5 (×4420).

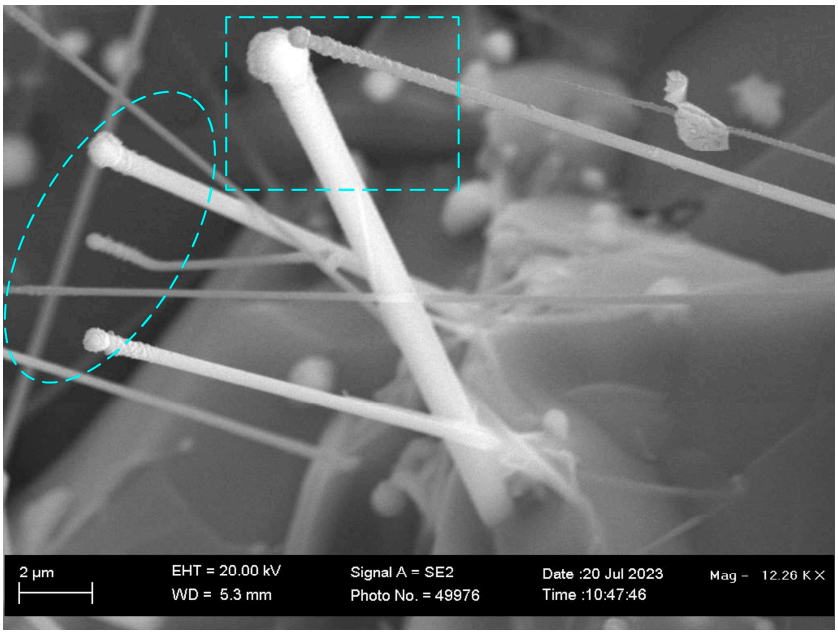

(**a**)

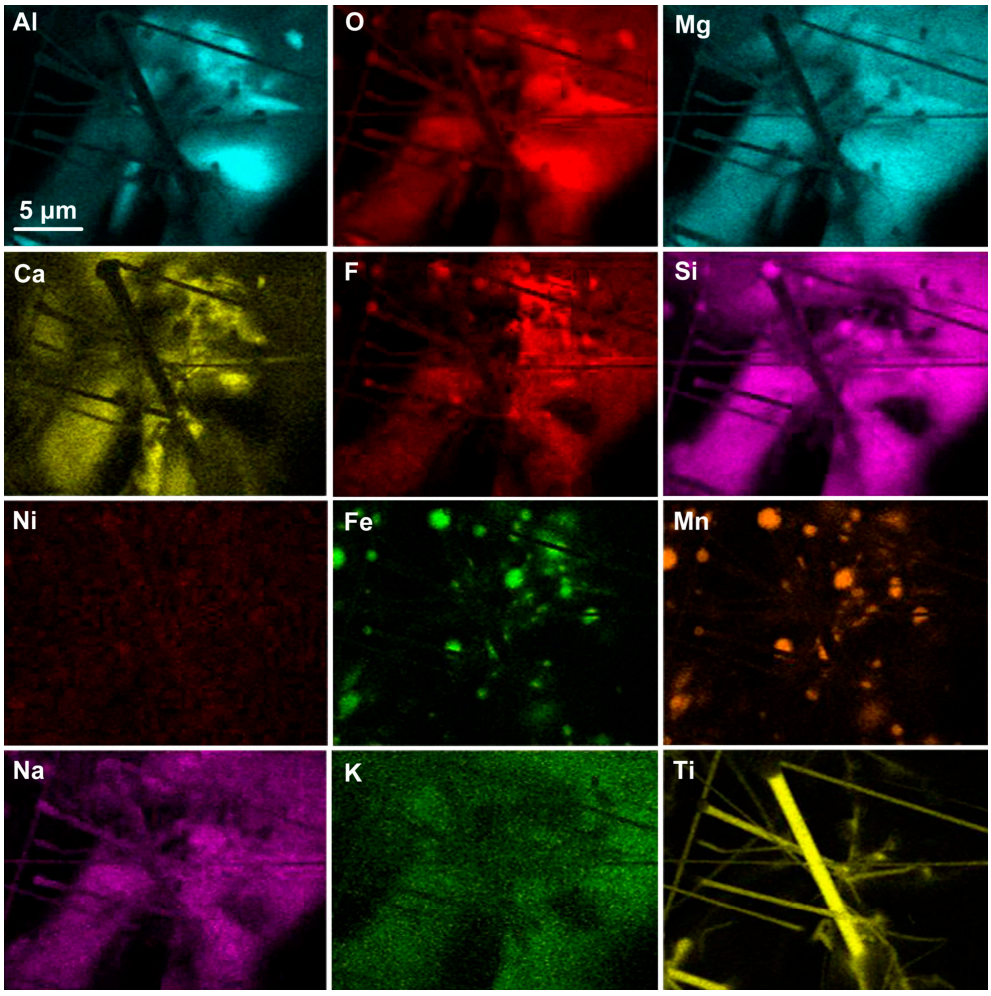

(**b**)

Figure 7. (**a**): SEM image (×12,260) of analysed area marked as blocked area in Figure 6; (**b**): EDX map of area in (**a**).

The end-caps in Figure 7 are dominated by Mn-Fe-Si fluoride, similar to the chemistry of the end-caps in Figure 4b. However, the end-caps in Figure 7 also contain Al-Mg-Na-O, as seen in the dashed-line oval area. The formation of oxy-fluoride end-caps agrees with prior observations in the reaction of Cr-Al-Fe metal powder [33]. The presence of Ni in the EDS maps in Figure 7b is unclear. Table 2 displays the average FOV analyses of Figures 3–7. It is seen that small amounts of Ni were analysed in Figures 3, 4 and 7. Maximum element standard deviation values (σ) are shown in Table 2, indicating the SEM-EDX analysis quality. The flux analysis from Table 1 is shown in the last line of Table 2. Similarly, the glass phase SEM-EDX analyses in post-weld slag from welding without metal powder additions are also shown in the second and third last lines of Table 2 [39]. The increased Ti content in each FOV analysis is of interest compared to the flux analysis in the last line in Table 1. Although the flux contains a low quantity of Ti of 0.6%, the formation of Ti nano-strands increases Ti content to 2.2–7.2% Ti in the FOV displayed in Figures 3, 4, 6 and 7.

Table 2. Average EDS field of view (FOV) analyses in Figures 3, 4, 6 and 7.

Figure	%O	%F	%Na	%Mg	%Al	%Si	%K	%Ca	%Ti	%Ni	%Mn	%Fe
3	42.9	8.7	1.4	15.9	14.5	5.4	0.2	4.1	2.2	0.03	2.1	2.2
4	44.7	7.7	1.5	12.2	16.8	5.7	0.3	3.4	2.3	0.04	2.4	2.8
6	40.7	8.3	1.9	11.2	11.2	7.6	0.6	3.8	5.5	0.00	5.2	3.5
7	43.2	9.4	2.2	11.3	11.3	8.3	0.7	3.4	7.2	0.02	2.6	1.7
Maximum σ	0.40	0.16	0.03	0.11	0.12	0.08	0.01	0.04	0.06	0.01	0.06	0.04
Glass [39]	34.3	12.3	2.0	12.4	6.8	12.1	0.3	12.8	0.6	0.0	5.7	0.7
Glass [39]	34.1	12.7	2.0	12.3	6.2	12.4	0.0	13.3	0.7	0.0	5.8	0.5
Flux	35.3	8.7	0.6	13.4	13.2	9.2	0.2	9.3	0.6	0.0	5.3	4.2

4. Discussion

According to the EDS maps in Figures 4b and 7b, the nano-strands consist predominantly of Ti. The only source of Ti in the reaction system is the TiO_2 compound in the flux, see Table 1. The nano-strands in Figure 4 are shorter than those in Figure 7. The nano-strands in Figure 4 have end-caps of Mn-Fe-Si fluoride, compared to Al-Mg-Na-Mn-Fe-Si oxy-fluoride in Figure 7. Also, the nano-strands in Figure 7 contain Al-Mg-Si-Na oxy-fluoride with Ti as the dominant element. In comparison, the nano-strands in Figure 4 contain only Ti. The authors' recent results identified the likely gas-phase-based reactions in Ti nano-strand formation [33–35]. Thermochemistry calculations showed that Ti displacement from the Ti-fluoride gas by the added Al powder proceeds according to reaction (1). Ti-fluorides (TiF_4, TiF_3, TiF_2, TiF) and Al-fluorides (AlF_3, AlF_2, AlF) are in the gas phase above 1300 °C.

$$yAl + xMF_y \leftrightarrow xM + yAlF_x \quad (1)$$

Similarly to reaction (1), the displacement of Ni from NiF_2 is also possible, indicating that Ni transfer via the gas phase is possible. From the low concentration of Ni in the FOV analyses, it seems that the extent of Ni vaporisation and re-condensation was limited under the experimental conditions applied here. The presence of oxy-fluoride in the nano-strands and nano-strand end-caps in Figure 7b indicates that oxygen-containing fluoride is also condensed. This is possible since AlOF gas can form from low-temperature oxy-fluoride reactions [2]. In addition, it is well documented that MgO nano-strands can form from pure MgO dissociated to Mg vapour and oxygen gas, thus incorporating the original oxygen from the MgO back into the MgO nano-strand instead of forming only a Mg nano-strand via the vapour–liquid–solid (VLS) and vapour–solid (VS) mechanisms [40–42]. The MgO starting material must be reacted at low-oxygen partial pressure, but the reaction temperature can vary from low temperatures (900 °C) to high temperatures (1600 °C) [40–42]. The VLS/VS

mechanisms are likely also at play in this work and can explain the method of oxygen incorporation into the nano-strands.

The proportion of Al reacted with the oxy-fluoride slag is not known. The following calculations were made to investigate the likely gas composition at the reaction of different proportions of Al. The gas–slag–metal equilibrium was calculated in FactSage 7.3 in the Equilib module for 1350 °C with the FactPS, Fstel, and FToxid databases selected [43]. The calculations were made for reactions of 3, 5, 7, and 9 mass% Al. The Ni and Fe metal powders were excluded from the calculations since initial runs indicated negligible influence on the equilibrium gas composition.

Figure 8a,b display the main gas-phase constituents from the equilibrium calculation, namely $KalF_4$, TiF_3, $NaAlF_4$, SiF_4, AlF_3, SiF_3, and Na. It is seen that the TiF_3 percentage decreases with increased Al reacted. This prediction agrees with reaction (1), proceeding with more Al reactant available to react with the TiF_3 to form AlF_3. This effect is summarised in the Ti mass distribution among the gas, slag, and alloy phases, as displayed in Figure 8c. It is seen that less TiF_3 remains in the gas as more Al is reacted, whilst the $KalF_3$ proportion increases. Zaitsev et al. [2] explained that the gas compounds $KalF_4$ and $NaAlF_4$ could be considered mixtures of the simple fluorides of KF or NaF and AlF_3, leading to a simplified gas composition expression. The calculated gas compositions confirm that the flux CaF_2, the only F source, is transformed into different fluoride gasses and oxy-fluoride glass phase in the slag. The generally accepted that CaF_2 reacts with oxides to convert to the metal fluorides via reactions similar to Equation (2) [11,44,45].

$$SiO_2(slag) + 2CaF_2(g) \leftrightarrow 2CaO(slag) + SiF_4(g) \quad (2)$$

The above thermochemistry calculations confirm that nano-strand formation likely occurs via gas-phase reactions. This conclusion agrees with previous studies showing that metal halides of I, Cl, and Br heated to 900 °C under a reducing gas atmosphere of hydrogen can decompose to form metal whiskers from vapour deposition [46,47]. However, in these studies, the formation of whiskers from fluoride was not observed under the same reaction conditions of a hydrogen atmosphere and a low temperature of 900 °C [46]. Therefore, in addition to the thermochemistry calculations above, the possibility of Ti nano-strand formation from the underlying oxy-fluoride glass is evaluated in the following section as diffusion calculations.

The calculations compare diffusion flux from the gas and glass phases to form a typical Ti nano-strand. The Ti flux required in forming the larger nano-strand in the centre of Figure 7a with a diameter of 0.5 µm and length of 13 µm was calculated as 3.39×10^{-3} mol/m^2·s, using the inputs in Table 3. This is the maximum value estimation because the strand is assumed to be pure Ti metal, although Figure 7b indicates the presence of Al-Mg-Si-Na-O-F. The Ti gas-phase and slag-phase diffusion fluxes were calculated and compared to the maximum diffusion flux of 3.39×10^{-3} mol/m^2·s. The assumptions in calculating the maximum diffusion flux are that the nano-strand consists of Ti metal of theoretical density and that the total reaction time of 6 min is applied as the diffusion time. Equation (3) is used to calculate the maximum diffusion flux:

$$J_{max} = (1000 \times V \times \rho)/(A \times t \times M_{Ti}) \quad (3)$$

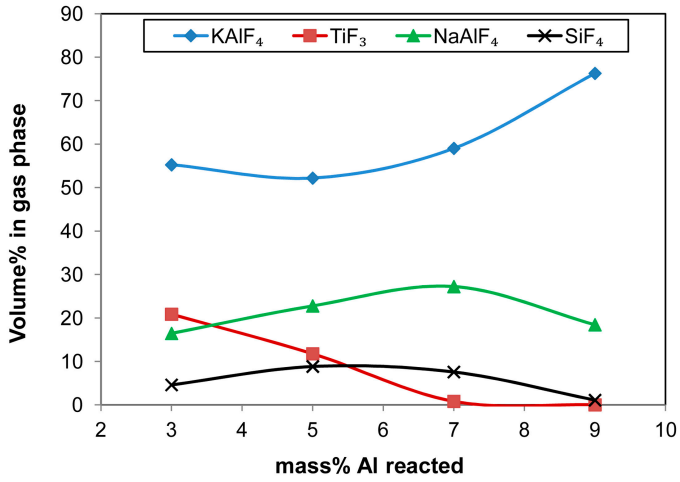

(**a**)

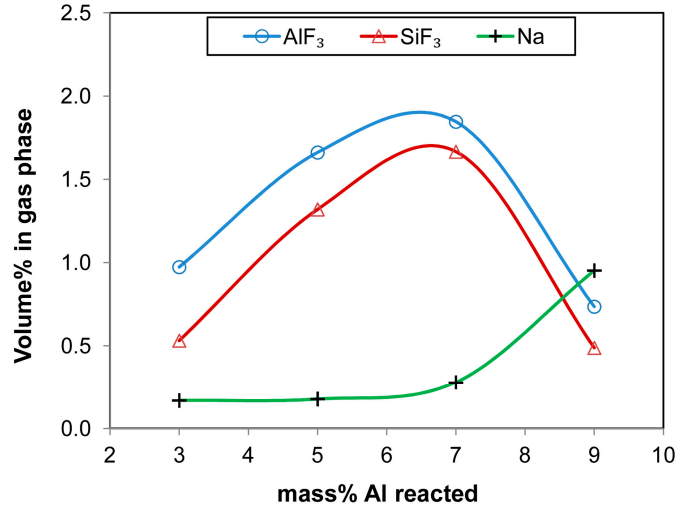

(**b**)

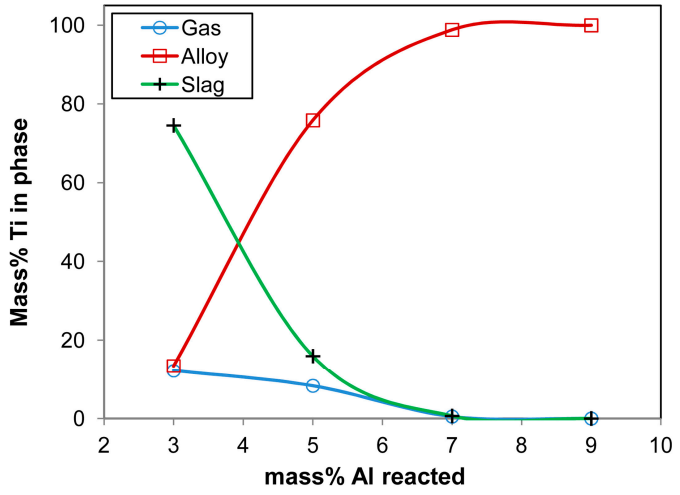

(**c**)

Figure 8. (**a**): Equilibrium gas composition under increased Al reaction: main species. (**b**): Equilibrium gas composition at increased Al reaction: minor species. (**c**): Titanium phase distribution under increased Al reaction.

Table 3. Maximum Ti diffusion flux calculations summary.

Description	Units	Symbol	Value
Strand length	m	X	13×10^{-6}
Strand diameter	m	D	0.5×10^{-6}
Strand volume	m^2	V	2.55×10^{-18}
Strand cross-section area	m^2	A	1.96×10^{-13}
Ti density [48]	kg/m^2	ρ	4500
Time	seconds	t	360
Ti mol mass	gram/mol	M_{Ti}	47.88
Mass Ti in strand volume	gram		1.15×10^{-11}
Ti diffusion flux	$mol/m^2 \cdot s$	J_{Max}	3.39×10^{-3}

The diffusion flux from the gas and glass phases was calculated using Fick's first law [49], as displayed in Equations (4) and (5).

$$J_{glass} = -D_{Ti} \times (\Delta C/\Delta X) \quad (4)$$

$$J_{gas} = -D_{Ti} \times (P_{Ti}/\Delta XRT) \quad (5)$$

J = diffusion flux [$mol/m^2 \cdot s$];
D = diffusion coefficient [m^2/s];
C = concentration [mol/m^3]
X = diffusion length [m];
R = gas constant= 8.3144 [$J/mol \cdot K$];
T = temperature [K].

The following assumptions were made in calculating the gas-phase diffusion flux: The maximum equilibrium partial pressure for TiF_3 is 0.21 atm, as in Figure 8a, and is used as the equivalent maximum Ti partial pressure. The diffusion distance is the nano-strand length of 13 µm. The gas-phase diffusion coefficient value is taken from the literature and reported as the lower end value in gas diffusion coefficients [50]. In the glass-phase diffusion flux calculation, the following assumptions were made. The volume of the glass phase participating in the nano-strand formation is equal to the nano-strand volume. The glass phase density is 2500 kg/m^2, the same as an Al_2O_3-CaF_2-MgO-SiO_2 slag [51]. The Ti concentration (mol/m^3) at the surface of the glass was calculated from the flux TiO_2 content of 1%, Table 1, and the glass mass contained in the same volume as that of the nano-strand. The diffusion distance is the nano-strand length of 13 µm. The diffusion coefficient value for Ti ions in glass was taken from the literature as the lower value for ionic diffusion of Si^{4+} and O^{2-} since Ti cations display similar behaviours in slags [52]. The calculation results in Table 4 show that the diffusion flux from the gas phase is orders of magnitude larger than that required for the maximum flux value, and the glass-phase diffusion flux is orders of magnitude smaller than the required value. These numbers support the conclusion that the nano-strand formation reactions are gas-phase-based and not glass-phase-based.

Table 4. Diffusion flux calculations results summary.

Scenario	Maximum Ti Diffusion Flux	Gas phase Ti Diffusion Flux	Glass Phase Ti Diffusion Flux
J [$mol/m^2 \cdot s$]	3.39×10^{-3}	1.21	9.63×10^{-7}
D_{Ti} [m^2/s]	not applied	1.00×10^{-5}	4.00×10^{-11}

The above results and discussion show that gas-phase reactions are involved in nano-strand formation in oxy-fluoride melts applicable to welding fluxes, even at low temperatures such as 1350 °C. Therefore, this low-temperature experimental technique is suitable as a simplified simulation experiment to study flux behaviours. The low vaporisation and

re-condensation extent of added Ni metal powder indicates that a longer reaction time may be necessary to examine the details of Ni vaporisation and re-condensation in the oxy-fluoride reaction system.

5. Conclusions

The low-temperature (1350 °C) simulation experiment applied here can be used to investigate the gas-phase behaviour of oxy-fluoride flux in reaction with added metal powders. This is concluded because nano-strand formation via the gas-phase mass transfer of specific elements confirms gas-phase reactions. Ti-dominated nano-strands, with predominantly Mn-Fe-Si fluoride end-caps formed quickly within a 6 min reaction time. The low volatilisation and re-condensation extent of added Ni metal powder indicates that a longer reaction time may be necessary for Ni metal powder-containing reaction systems. The Ti-dominated nano-strands likely formed via the gas-phase-based displacement of Ti from TiF_3 gas. The increased reaction of Al with gas leads to modified gas compositions and increased Ti formation. The calculated Ti diffusion flux values for gas-phase and glass-phase diffusion, compared to the maximum Ti diffusion flux required to form a typical nano-strand, confirm that gas-phase reactions present the likely nano-strand formation mechanism.

Author Contributions: F.D.B. conceptualised the work; F.D.B. and T.C. executed the experiments together, and interpreted the data together, and prepared the manuscript together. All authors have read and agreed to the published version of the manuscript.

Funding: This research was funded in part by the University of Pretoria.

Data Availability Statement: The data sets presented in this study are available upon reasonable request to the corresponding author, as indicated on the first page.

Acknowledgments: The authors are grateful to Erna van Wilpe and Coenraad Snyman at the Laboratory for Microscopy and Microanalysis at the University of Pretoria for their advice and assistance on SEM imaging and analysis in this work.

Conflicts of Interest: The authors declare no conflicts of interest. The funders had no role in the design of the study; in the collection, analyses, or interpretation of the data; in the writing of the manuscript, or in the decision to publish the results.

References

1. Linnert, G.E. *Welding Metallurgy-Carbon and Alloy Steels, Volume I-Fundamentals*, 4th ed.; American Welding Society (AWS): Miami, FL, USA, 1994; pp. 706–758.
2. Zaitsev, A.I.; Leites, A.V.; Litvina, A.D.; Mogutnov, B.M. Investigation of the mould powder volatiles during continuous casting. *Steel Res.* **1994**, *65*, 368–374. [CrossRef]
3. Ju, J.; Ji, G.; An, J.; Tang, C. Effect if TiO_2 on fluoride evaporation from CaF_2-CaO-Al_2O_3-MgO-Li_2O-(TiO_2) slag. *Ironmak. Steelmak.* **2020**, *48*, 109–115. [CrossRef]
4. Gao, J.; Wen, G.; Liu, Q.; Tan, W.; Tang, P. Effect of Al_2O_3 on the fluoride volatilization during melting and ion release in water of mould flux. *J. Non-Cryst. Solids* **2015**, *409*, 8–13. [CrossRef]
5. Ju, J.; Gu, Y.; Zhang, Q.; He, K. Effect of CaF_2 and CaO/Al_2O_3 ratio on evaporation and melting characteristics of low-fluoride CaF_2-CaO-Al_2O_3-MgO-TiO_2 slag for electroslag remelting. *Ironmak. Steelmak.* **2023**, *50*, 13–20. [CrossRef]
6. Persson, M.; Seetharaman, S.; Seetharaman, S. Kinetic studies of fluoride evaporation from slags. *ISIJ Int.* **2007**, *47*, 1711–1717. [CrossRef]
7. Schulz, T.; Lychatz, B.; Haustein, N.; Janke, D. Structurally based assessment of the influence of fluorides on the characteristics of continuous casting powder slags. *Metall. Trans. B* **2013**, *44*, 317–327. [CrossRef]
8. Krasovskyy, V.P. Interaction of single-crytalline metal fluorides with titanium-containing melts. *Powder Metall. Met. Ceram.* **2019**, *58*, 334–340. [CrossRef]
9. Chai, C.S.; Eagar, T.W. Slag-metal equilibrium during submerged arc welding. *Metall. Trans. B* **1981**, *12*, 539–547. [CrossRef]

10. Mitra, U.; Eagar, T.W. Slag-metal reactions during welding: Part I. Evaluation and reassessment of existing theories. *Metall. Trans. B* **1991**, *22*, 65–71. [CrossRef]
11. Chai, C.S.; Eagar, T.W. Slag metal reactions in binary CaF_2-metal oxide welding fluxes. *Weld. J.* **1982**, *61*, 229–232.
12. Polar, A.; Indacochea, J.E.; Blander, M. Electrochemically generated oxygen contamination in submerged arc welding. *Weld. J.* **1990**, *69*, 68–74.
13. Lau, T.; Weatherly, G.C.; Mc Lean, A. The sources of oxygen and nitrogen contamination in submerged arc welding using CaO-Al_2O_3 based fluxes. *Weld. J.* **1985**, *64*, 343–347.
14. Kim, J.H.; Frost, R.H.; Olson, D.L.; Blander, M. Effect of electrochemical reactions on submerged arc weld metal compositions. *Weld. J.* **1990**, *69*, 446–453.
15. Davis, M.L.E.; Bailey, N. Evidence from inclusion chemistry of element transfer during submerged arc welding. *Weld. J.* **1991**, *70*, 57–61.
16. O'Brien, A. *Welding Handbook—Welding Processes, Part 1*, 9th ed.; American Welding Society (AWS): Miami, FL, USA, 2004; Volume 2.
17. Coetsee, T.; De Bruin, F. Aluminium-Assisted Alloying of Carbon Steel in Submerged Arc Welding with Al-Cr-Ni Unconstrained Metal Powders: Thermodynamic Interpretation of Gas Reactions. *Processes* **2022**, *10*, 2265. [CrossRef]
18. Bailey, N. Submerged arc welding ferritic steels with alloyed metal powder. *Weld. J.* **1991**, *70*, 187–206.
19. Tušek, J.; Suban, M. High-productivity multiple-wire Submerged-Arc Welding and cladding with metal-powder addition. *J. Mater. Process. Technol.* **2003**, *133*, 207–213. [CrossRef]
20. Nand, S.; Singh, P.K. Effect of addition of metal powder on deposition rate, mechanical properties, and metallographic property of weld joints during Submerged Arc Welding process. *J. Mach. Form. Technol.* **2015**, *6*, 159–168.
21. Bong, W.L. System and Method for Metal Powder Welding. U.S. Patent 8946582 B1, 3 February 2015.
22. Hallén, H.; Johansson, K.-E. Use of a Metal Powder for Surface Coating by Submerged Arc Welding. U.S. Patent 6331688 B1, 18 December 2001.
23. Patel, D.; Soman, S.N. Develop a flux cored wire for submerged arc welding of Ni-Mo low alloy steel. *Sadhana* **2020**, *45*, 127. [CrossRef]
24. Allen, J.W.; Olson, D.L.; Frost, R.H. Exothermically assisted shielded metal arc welding. *Weld. J.* **1998**, *77*, 277–285.
25. Trembach, B.; Grin, A.; Subbotina, V.; Vynar, V.; Knyazev, S.; Sakiev, V.; Trembach, I.; Kabatsky, O. Effect of exothermic addition (CuO-Al) in the structure, mechanical properties and abrasive wear resistance of the deposited metal during self-shielded flux-cored arc welding. *Tribol. Ind.* **2021**, *43*, 452–464. [CrossRef]
26. Trembach, B.; Grin, A.; Turchanin, M.; Makarenki, N.; Markov, O.; Trembach, I. Application of taguchi method and ANOVA analysis for optimization of process parameters and exothermic addition (CuO-Al) introduction in the core filler during self-shielded flux-cored arc welding. *Int. J. Adv. Manuf.* **2021**, *114*, 1099–1118. [CrossRef]
27. Lozynskyi, V.; Trembach, B.; Katinas, E.; Sadovyi, K.; Krbata, M.; Balenko, O.; Krasnoshapka, I.; Rebrova, O.; Knyazev, S.; Kabatskyi, O.; et al. Effect of Exothermic Additions in Core Filler on Arc Stability and Microstructure during Self-Shielded, Flux-Cored Arc Welding. *Crystals* **2024**, *14*, 335. [CrossRef]
28. Kaplan, H.I.; Hill, D.C. Thermodynamics of air-operating flux cored electrodes and an analysis of weld toughness. *Weld. J.* **1976**, *55*, 13–19.
29. Sasaki, Y.; Nagai, Y.; Ikemoto, K.; Suga, T.; Sato, M. Flux Cored Wire electrodes for Self-Shielded Arc Welding. U.S. Patent 4571480, 18 February 1986.
30. Babu, S.S.; David, S.A.; Quintana, M.A. Modeling microstructure development in self-shielded flux cored arc welds. *Weld. J.* **2001**, *80*, 91–97.
31. Sengupta, V.; Havrylov, D.; Mendez, P.F. Physical phenomena in the weld zone of submerged arc welding—A Review. *Weld. J.* **2019**, *98*, 283–313.
32. Gött, G.; Gericke, A.; Henkel, K.-M.; Uhrlandt, D. Optical and spectroscopic study of a submerged arc welding cavern. *Weld. J.* **2016**, *95*, 491–499.
33. Coetsee, T.; De Bruin, F. Low temperature vaporisation of Cr from fluoride flux reacted at 1350 °C with Al–Cr–Fe powder: Thermochemical analysis of gas phase reactions and nano-strand formation. *J. Mater. Res. Technol.* **2024**, *30*, 1159–1171. [CrossRef]
34. Coetsee, T.; De Bruin, F. Nano-strand formation in CaF_2-SiO_2-Al_2O_3-MgO flux reacted at 1350 °C with Al-Ti-Fe powder: SEM analyses and gas reaction thermochemistry. *J. Solid State Chem.* **2024**, *331*, 124547. [CrossRef]
35. Coetsee, T.; De Bruin, F. Nano-Strand Formation via Gas Phase Reactions from Al-Co-Fe Reacted with CaF_2-SiO_2-Al_2O_3-MgO Flux at 1350 °C: SEM Study and Thermochemistry Calculations. *Processes* **2024**, *12*, 1342. [CrossRef]
36. Coetsee, T.; De Bruin, F. Insight into the Chemical Behaviour of Chromium in CaF_2-SiO_2-Al_2O_3-MgO Flux Applied in Aluminium-Assisted Alloying of Carbon Steel in Submerged Arc Welding. *Minerals* **2022**, *12*, 1397. [CrossRef]

37. Coetsee, T.; De Bruin, F. EERZ (Effective Equilibrium Reaction Zone) Model of Gas-Slag-Metal Reactions in the Application of Unconstrained Al-Ni-Cr-Co-Cu Metal Powders in Submerged Arc Welding: Model and 3D Slag SEM Evidence. *Processes* **2023**, *11*, 2110. [CrossRef]
38. Coetsee, T.; Mostert, R.J.; Pistorius, P.G.H.; Pistorius, P.C. The effect of flux chemistry on element transfer in Submerged Arc Welding: Application of thermochemical modelling. *J. Mater. Res. Technol.* **2021**, *11*, 2021–2036. [CrossRef]
39. Coetsee, T. Phase chemistry of Submerged Arc Welding (SAW) fluoride based slags. *J. Mater. Res. Technol.* **2020**, *9*, 9766–9776. [CrossRef]
40. Yamaguchi, A.; Hashimoto, S. Growth if magnesia whiskers. *Ceram. Int.* **1992**, *18*, 301–305. [CrossRef]
41. Zhao, M.; Chen, X.L.; Wang, W.J.; Ma, Y.J.; Xu, Y.P.; Zhao, H.Z. Self-catalyzed growth if magnesium oxide nanorods. *Mater. Lett.* **2006**, *60*, 2017–2019. [CrossRef]
42. Kumar, D.; Pistorius, P.C. Use of slag (CaO-Al_2O_3-SiO_2-MgO) droplet as a catalyst to grow MgO whiskers through VLS machanism. *Ceram. Int.* **2017**, *43*, 15478–15485. [CrossRef]
43. Bale, C.W.; Bélisle, E.; Chartrand, P.; Decterov, S.A.; Eriksson, G.; Gheribi, A.E.; Hack, K.; Jung, I.-H.; Kang, Y.-B.; Melançon, J.; et al. Reprint of: FactSage thermochemical software and databases, 2010–2016. *Calphad* **2016**, *55*, 1–19. [CrossRef]
44. Lau, T.; Weatherly, G.C.; Mc Lean, A. Gas/Metal/Slag reactions in Submerged Arc Welding using CaO-Al_2O_3 based fluxes. *Weld. J.* **1986**, *65*, 31–38.
45. Shinmei, M.; Machida, T. Vaporization of AlF_3 from the slag CaF_2-Al_2O_3. *Metall. Trans.* **1977**, *4*, 1996–1997. [CrossRef]
46. Brenner, S.S. The growth of whiskers by the reduction of metal salts. *Acta Metall.* **1956**, *4*, 62–74. [CrossRef]
47. Brenner, S.S.; Sears, G.W. Mechanism of whisker growth-III Nature of growth sites. *Acta Metall.* **1956**, *4*, 268–270. [CrossRef]
48. Brandes, E.A.; Brook, G.B. *Smithells Metals Reference Book*, 7th ed.; Butterworth-Heinemann: Oxford, UK, 1992.
49. Callister, W.C., Jr.; Rethwisch, D.G. *Callister's Materials Science and Engineering*, 10th ed.; Global Edition; John Wiley & Sons: West Sussex, UK, 2019; pp. 132–149.
50. Poirier, D.R.; Geiger, G.H. *Transport Phenomena in Materials Processing*; TMS: Warrendale, PA, USA, 1994; pp. 453–456.
51. Allibert, M.; Verein Deutscher Eisenhüttenleute. *Slag Atlas*, 2nd ed.; Verlag Stahleisen: Düsseldorf, Germany, 1995; p. 340.
52. Turkdogan, E.T. *Fundamentals of Steelmaking*; The Institute of Materials: Cambridge, UK, 1996; pp. 176–177.